CHEMISTRY OF MATERIALS

ARTICLE

pubs.acs.org/cm

Sequential Vapor Infiltration of Metal Oxides into Sacrificial Polyester Fibers: Shape Replication and Controlled Porosity of Microporous/Mesoporous Oxide Monoliths

Bo Gong, Qing Peng, Jesse S. Jur, Christina K. Devine, Kyoungmi Lee, and Gregory N. Parsons*

Department of Chemical and Biomolecular Engineering, North Carolina State University, Raleigh, North Carolina 27695, United States

ABSTRACT: The preparation of microporous and mesoporous metal oxide materials continues to attract considerable attention, because of their possible use in chemical separations, catalyst support, chemical sensors, optical and electronic devices, energy storage, and solar cells. While many methods are known for the synthesis of porous materials, researchers continue to seek new methods to control pore size distribution and macroscale morphology. In this work, we show that sequential vapor infiltration (SVI) can yield shape-controlled micro/mesoporous materials with tunable pore size, using polyesters as a sacrificial template. The reaction proceeds by exposing polymer fiber templates to a controlled sequence of metal organic and co-reactant vapor exposure cycles in an atomic layer deposition (ALD) reactor. The precursors infuse sequentially and thereby distribute and react uniformly within the polymer, to yield an organic−inorganic hybrid material that retains the physical dimensions of the original polymer template. Subsequent calcination in air results in an inorganic microporous/mesoporous material that again retains the macroscopic physical shape of the starting polymer matrix. The microporous/mesoporous structure is confirmed by microscopy and nitrogen adsorption/desorption analysis, and the resulting pore size is controlled by the size of the starting polymer repeat unit and by the kinetics of the infiltration/annealing process steps. In situ infrared transmission and quartz crystal microbalance results confirm the chemical reaction mechanisms. The chemical transformation that occurs during SVI could be important for a range of applications that utilize well-defined porous nanostructures.

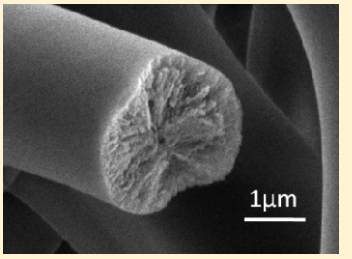

KEYWORDS: porous material, metal oxide, aluminum oxide, titanium oxide, atomic layer deposition, vapor phase infiltration

I. INTRODUCTION

Nanoporous materials are critical in many advancing technologies, including chemical separations, catalysis, chemical sensors, optical and electronic devices, energy storage, and solar energy conversion cells.[1,2] Porous materials are often prepared by solution-based methods, including sol−gel and hydrothermal processes, using structure-directed templates, such as surfactants and amphiphilic block copolymers, to control pore size distribution and surface area.[3,4] In addition, self-recognition and self-assembly chemistry can readily integrate with these processes to prepare new types of porous materials, including organic frameworks,[5−8] covalent organic frameworks,[9−11] intrinsic porous polymers,[12−14] and porous molecular cages.[15−18] A common drawback is that most methods require aqueous or organic solvents and long synthesis and processing times. Moreover, the material morphology that results from these methods is limited to powders.[19] New methods that can produce continuous porous materials with well-defined pore size distribution, while simultaneously enabling material structures with predetermined macroscale size, shape, and contour could enable new device functionality, such as defect-free gas separation modules and structured porous materials for drug delivery, chemical sensing, and energy storage and conversion.

Organic−inorganic hybrid templates are known to work well as sacrificial templates for inorganic porous structures with predefined macro morphology.[20,21] Calcination of the hybrid material generates a purely inorganic compound, with a form and shape that replicates the starting polymer. In order to prepare hybrid materials from solid polymer templates, researchers have developed several solution-based infiltration methods.[22,23] Unfortunately, solvents often lead to swelling and dissolution of the starting polymer, and careful control of the pH and humidity are needed to slow the reactions to disperse the metal oxide within the polymer matrix uniformly.

Vapor processing provides a solvent-free environment for the chemical modification of organic structures where water can be controlled at the parts per million scale or better. Reagent exposure pressure, time, and temperature are also readily adjusted. Recent studies of vapor-phase surface modification of polymers by inorganic atomic layer deposition (ALD)[24−26] demonstrated that metal oxide precursors often diffuse subsurface into the polymer, creating a graded organic/inorganic interface region. The extent of subsurface diffusion and deposition during ALD on polymers is known to be affected by reaction temperature, the extent of precursor exposure, and the specific chemical interactions between the precursors and reactive groups in the polymer.[24−26] Other studies show that vapor infiltration alters the chemical and mechanical properties of natural polymer

Received: March 8, 2011
Revised: June 7, 2011
Published: July 18, 2011

materials.[27,28] We can promote subsurface species diffusion and reaction during vapor exposure, for example, by carefully selecting the polymer template, metal-organic precursor, and the extent of precursor exposure.

In this work, we show that, by allowing the subsurface precursor diffusion/reaction and sequence co-reactant diffusion to approach saturation, we can produce a homogeneous organic–inorganic hybrid material that retains the form and shape of the starting polymer template. Calcination yields a porous inorganic solid with pore size and pore size distribution controlled by the details of the infiltration and calcination process steps, where, again, the shape of the resulting solid matrix directly mimics the starting nonwoven polymer fiber web. Specifically, we examine the detailed reaction processes during the infiltration and reaction of metal-organic precursors (such as trimethyl aluminum and titanium tetrachloride) with various polyester fibers, resulting in a set of different covalently coordinated organic–inorganic solid cylindrical matrices. The reaction proceeds in common ALD processing equipment, in an environment with well-controlled pressure and temperature, where the metal-organic exposure is typically followed by an inert gas purge and a subsequent co-reactant exposure step. We also report the relationship between the reactant exposure time, the temperature, and the extent of reaction between the polymer and the reactants, and how the details of the reaction and annealing conditions affect pore distribution. Using higher temperature and longer infiltration times during metal-organic exposure, we find that the pore size shrinks and the size distribution narrows, where the size approaches the monomer unit dimension in the starting polymer. This indicates that polymer molecular structure acts to template the porous oxide structure. Thus, by choosing the starting polyester monomer length, the pore size could be preselected and adjusted which will be useful for separations, vapor adsorption, and other important applications.

II. EXPERIMENTAL PROCEDURES

Chemicals and Materials. All materials and chemicals were purchased commercially and used as received. Trimethyl aluminum (TMA, 95%) and diethyl zinc (DEZ, 98%) were purchased from Strem Chemicals, and titanium tetrachloride (TCl_4, 99%) was purchased from Gelest. The oxygen source was deionized water. The reactant carrier and purge gas was ultrahigh-purity argon (99.999%) (National Welders), and it was further purified using a Gatekeeper inert gas purifier (rated to <100 parts per trillion H_2O and O_2) before flowing into the reactor. For infrared (IR) transmission studies on planar deposited films, we used double-side-polished high-resistivity (50–100 Ω cm) *n*-type Si(100) wafer substrates to provide uniform 60% IR transmittance over the middle IR region. Before use, all silicon wafers were first cleaned by dipping them into a JTP cleaning solution for 2 min, followed by 5 min of a deionized water flow rinse, and then they were dried under a high-purity (99%) nitrogen flow. Polybutylene terephthalate (PBT), polyethylene terephthalate (PET), polylactic acid (PLA), and polyethylene naphthalate (PEN) nonwoven fiber mats were acquired from the Nonwoven Cooperative Research Center at North Carolina State University. Trifluorine acetic acid (TFA) and PBT pellets (molecular weight (MW) of ~38 000) were purchased from Sigma–Aldrich.

Reactor and In Situ Analysis. Sequential vapor infiltration (SVI) of TMA, $TiCl_4$, and water into the polymer substrates was carried out in a homemade viscous flow atomic layer deposition (ALD) reactor, as described previously.[29] The working pressure in the reactor during gas purge cycle was ~1 Torr. A typical SVI process used a sequence of 60 exposure steps, where each exposure step included flowing TMA into the reactor for 10 s, followed by sealing the reactor at fixed pressure (~2 Torr) for 60 s, then purging the reactor with argon for 20 s. This sequence corresponded to one TMA "soak" cycle. After 60 TMA soak steps (a total soak time of 1 h), the reactor was purged with argon for 15 min, then 20 water soak steps were performed using the same timing sequence before removing the sample from the reactor. For some fiber samples, a long continuous soak scheme was used, which included exposing the sample to ~7 Torr of TMA or $TiCl_4$ vapor for ~18 h, followed by a purge with argon for 30 min and a soak in 5 Torr of water vapor for ~1 h.

We equipped the reactor with in situ quartz crystal microbalance (QCM) sensor and used it to monitor mass uptake during the reactant exposures. For this experiment, PBT polymer pellets were dissolved in trifluorine acetic acid, and an ~200 nm thick PBT film was spun-coat onto a QCM crystal. The crystal is then mounted to the QCM housing, using conductive silver epoxy. The QCM head was then positioned in the reaction chamber at the center deposition site. The sensor head was modified to allow inert gas flow (~10 sccm) to the backside of the QCM crystal to locally prevent film deposition and protect the electrical contacts. A film thickness monitor (Maxtek TM-400) recorded the mass change using a Labview program. The QCM setup is very sensitive to the temperature and environmental pressure, so to ensure that the temperature and pressure were stable within the reactor, the reactor with the QCM setup was allowed to be purged with argon for several hours before collecting data.

A second reactor, which has also been described elsewhere,[30] was designed and equipped for in situ IR transmission analysis. It permitted the collection and analysis of Fourier transform infrared (FTIR) transmission spectra during the purge cycle after the soak steps, without removing the sample from the reactor. For these studies, we spun-coat PBT films on silicon IR substrates, using PBT polymer pellets dissolved in trifluorine acetic acid. A Thermo Scientific Model Nicolet 6700 IR system with an external MCT-A detector was used for the in situ FTIR analysis. The spectrometer operated in transmittance mode in the frequency range from 4000 cm^{-1} to 650 cm^{-1}. Spectra were collected at 4 cm^{-1} resolution, using 200 scans, corresponding to a data collection time of ~2 min per spectrum. A reference IR spectrum of the substrate was collected before the initial reactant dose. To better visualize the chemical reactions upon reactant exposure, all spectra are displayed in differential mode, where the previously collected spectrum was subtracted as the reference.

After infiltrating the polymer with the metal-organic precursor, calcination removed the organic species to produce the porous inorganic solid. The samples were heated in air for 12 h to achieve full calcination. During heating, the temperature was carefully ramped at 10 °C/min to ensure temperature uniformity.

Post-Reaction Characterization. The morphology of polymer fibers as received, after sequential vapor infiltration, and after calcination was imaged using scanning electron microscopy (SEM) (FEI Model XL30). Before imaging, samples were sputter-coated with ~5 nm of gold/palladium, to prevent charging. The SEM system operated at a voltage of 7 kV with a working distance of 5 mm. For cross-sectional imaging, we used a transmission electron microscopy (TEM) system (Hitachi Model HF 2000 cold-field-emission TEM microscope) that was capable of 0.2-nm point resolution operated at 200 kV. The TEM system is also equipped with an Oxford Link INCA energy-dispersive X-ray spectroscopy (EDS) apparatus, which was used to evaluate elemental composition during TEM analysis. The TEM samples were prepared using a Model Quanta 200 3D focused-ion-beam system.

The surface area, pore volume, and average pore size of the resulting materials were measured to quantify the nature of the porous material formed after sample calcination. We measured pore size distribution and surface area using a Quantachrome Autosorb-1C apparatus that was equipped with the ASWin software package. Nitrogen adsorption/

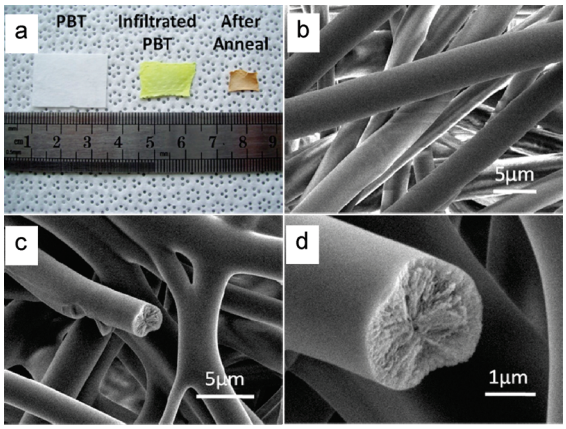

Figure 1. (a) Picture of polybutylene terephthalate (PBT) nonwoven fiber mats ((left) as-received, (middle) after TMA/water infiltration, and (right) after infiltration and anneal at 450 °C). The starting size for all samples was approximately the same. After infiltration, the fiber mat becomes yellow in color, shrinks in size, and becomes mechanically stiffer. Annealing causes more shrinkage, and the sample becomes more brittle, which is consistent with transformation of the polymer to micrometer-sized alumina fibers. (b) Scanning electron microscopy (SEM) image of the as-received PBT nonwoven. (c,d) SEM images showing similar samples after 1 h of TMA/water soaking and 12 h of annealing at 450 °C; the images in panels c and d show that the soaking and annealing preserves the starting fiber morphology. Some connectivity between the fibers likely results from polymer flow during the soaking process. More connectivity was observed with higher process temperature and longer precursor exposure. The cross-sectional view in panel d confirms that the fibers are uniform after calcination, indicating full penetration of the precursor throughout the 3-μm-diameter starting fiber.

desorption isotherms were performed using ~30 mg of sample and a 40-point adsorption/desorption scheme with standard micropore analysis ($2 \times 10^{-6} \leq P/P^{\circ} \leq 1.0$). Before analysis, the sample was allowed to outgas at 350 °C at the outgas port of the Autosorb 1 for more than 4 h. Surface areas were calculated by applying Brunauer–Emmett–Teller (BET) theory over the linear region of the isotherm ($0.05 \leq P/P^{\circ} \leq 0.30$). Pore size distributions were calculated in the ASWin software package using the nonlocal density functional theory method with the slit pore carbon equilibrium transition kernel. In addition to the N_2 adsorption/desorption analysis, similar experiments employing hydrogen allowed us to evaluate the hydrogen storage capability of the porous oxides.

We performed X-ray photoelectron spectroscopy (XPS) analysis using a Riber XPS system with a monochromatic Al Kα source. The pass energies for the survey and detail scans were 160 and 20 eV, respectively. For normalization, we set the adventitious C 1s peak to 284.5 eV. X-ray diffraction (XRD) studies employed a Philips Model Xpert Pro MRD HR X-ray diffraction system to determine the atomic structure of the starting PBT polymer, as well as the organic–inorganic materials.

We also performed differential scanning calorimetry (DSC) and thermogravimetric analysis (TGA) on vapor-phase-infiltrated organic–inorganic materials. A TA Instruments Model DSC Q2000 system was employed to measure the heat flow of untreated PBT fiber and TMA/water soaked PBT fiber in the temperature range from 0 °C to 275 °C. A TA Instruments Model TGAs-Q5000 system was used to test the mass loss upon heating for the untreated and TMA/water-soaked PBT fiber up to 900 °C. Before each set of TGA tests, calibration runs were recorded using 10–15 mg of platinum plate, freshly cleaned and annealed under a propane torch. The temperature ramp speed was typically fixed at 10 °C/min.

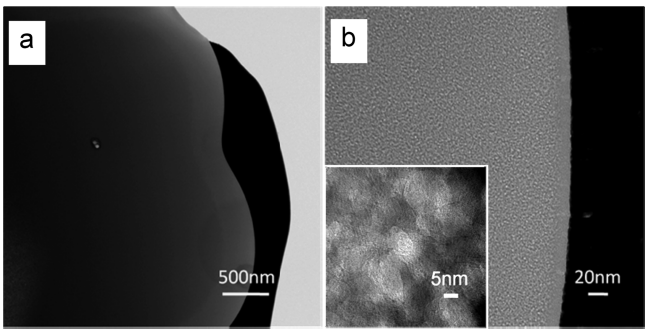

Figure 2. Cross-sectional TEM images of a PBT fiber after 1 h of TMA/water exposure at 80 °C and annealing at 450 °C. The dark region on the lower-resolution image is platinum deposited during TEM sample preparation. Some contrast in the image shown in panel a in the radial direction may be present. In panel b, a closer look of the outer edge of the fiber shows a uniformly distributed mesoporous structure. The inset shows a high magnification of the mesoporous structure, and it is consistent with a pore diameter of 5–10 nm.

III. RESULTS AND DISCUSSION

Imaging and Nitrogen Adsorption/Desorption Analysis of Post-Annealed Materials. Figure 1a shows a photograph of an untreated PBT nonwoven fiber mesh, a similar piece of nonwoven fiber after sequential vapor infiltration, and a similarly sized piece again after high-temperature calcination. Note that each treatment step produces a decrease in overall sample dimension. The brownish color after annealing is likely due to a small amount of carbon residue remaining in the sample. Figure 1b presents an SEM image of the untreated nonwoven PBT, showing a uniform mat of randomly distributed individual fiber units with a diameter of ~5 μm. Figures 1c and 1d show similar fibers after a TMA (60 min)/H_2O (20 min) vapor soak at 80 °C, followed by 24 h of calcination in air at 450 °C. After treatment, the macroscopic fiber diameter is smaller, but the overall macroscopic structure is not significantly changed. Figure 1c shows some connectivity between fibers after treatment that was not present previously. Some polymer flow could be expected due to polymer chain scission and/or local heating during the TMA/polymer reaction. A broken fiber in Figure 1d clearly shows a uniform cross section after high-temperature calcination. As will be shown below, the treatment process effectively converts the fibers from a polymer to a highly porous inorganic solid. The images in Figure 1 show that the material transformation largely maintains the macroscopic fibrous shape and framework of the original starting polymer. The polymer flow and interconnection in Figure 1c is consistent with polymer chain scission during TMA infiltration and reaction. The overall conversion process involves TMA/PBT reaction, followed by metal-organic ligand oxidation (during water exposure) and organic combustion (during post-treatment calcination). The uniform cross section after high-temperature calcination supports the conclusion that TMA permeates individual fibers and reacts throughout the PBT polymer fiber bulk.

Cross-sectional TEM images in Figure 2 show the fiber cross section on a relatively large scale (Figure 2a), as well on a more-detailed level (Figure 2b and inset) for PBT fibers after TMA/water SVI and calcination treatments. Some contrast in the fiber radial direction may be present in the image in Figure 2a, suggesting a small density gradient. At higher magnification,

dx.doi.org/10.1021/cm200694w |*Chem. Mater.* 2011, 23, 3476–3485

Table 1. Summary of Porous Metal Oxide Samples Prepared by Vapor Phase Infiltration

reactants	polymer fiber	infiltration temp (°C)	anneal temp (°C)	soak time (h)	BET surface area (m^2/g)	total pore volume (m^3/g)	mode pore width[a] (nm)
	PBT				0.71		
TMA/water	PBT	80	100	18	182.6	0.139	2.69
TMA/water	PBT	80	450	18	439.9	0.342	3.23
TMA/water	PBT	80	800	18	167.6	0.237	3.88
TMA/water	PBT	80	450	1	248.6	0.245	5.45
TMA/water	PBT	40	450	18	394.6	0.398	3.54
TMA/water	PBT	120	450	18	226.1	0.166	2.67
TMA/water	PBT	160	450	18	384.6	0.413	1.75
TMA/water	PLA	80	450	18	283.7	0.265	1.41
TMA/water	PET	80	450	18	280.9	0.172	1.49
TMA/water	PEN	80	450	18	396.1	0.289	2.68
$TiCl_4$/water	PBT	160	450	18	149.5	0.220	4.19
$TiCl_4$/water	PEN	160	450	18	208.2	0.334	3.63

[a] Mode pore width of TMA/water and $TiCl_4$/water soaked polyester fibers.

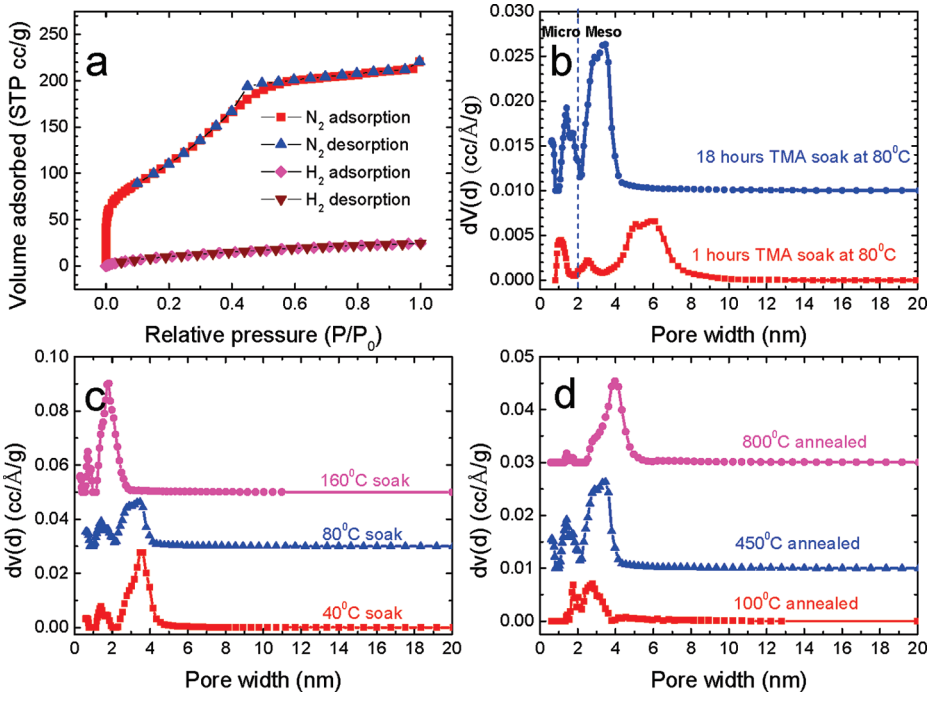

Figure 3. Nitrogen/hydrogen adsorption/desorption results collected at 77 K from PBT samples. (a) Nitrogen and hydrogen isotherm from PBT samples after 18 h of TMA/water soaking at 80 °C and 24 h of annealing at 450 °C; the hydrogen adsorption/desorption analysis shows an adsorption of 24.4 sccm/g at atmosphere pressure, corresponding to ~0.22 wt % hydrogen. (b) Pore size distribution results from PBT soaked in TMA vapor with different duration, with fixed infiltration (80 °C) and post-annealing temperature (450 °C); the longer soak time leads to smaller pores and higher pore volume, which is consistent with more TMA incorporation. (c) Pore size distribution results from PBT soaked in TMA vapor at different temperatures, with other conditions being fixed (see Table 1); higher soaking temperature also results in porous alumina with smaller pores, which is attributed to the increased reactivity between the TMA and the polymers. (d) Additional pore size analysis for PBT samples annealed at different temperatures after soaking under same condition (see details given in Table 1). The higher anneal temperature produces larger pores.

Figure 2b shows a uniform distributed mesoporous structure. It is also possible that a thin layer of Al_2O_3 might be formed on the polymer surface during the water pulse, hindering further diffusion of water into the polymer bulk. However, we believe that the outward diffusion of volatile products during water exposure (as discussed below) helps to produce pathways for water infiltration through any outer shell. Polymer surface−bulk exchange could further promote distribution of TMA into the polymer bulk.

dx.doi.org/10.1021/cm200694w |*Chem. Mater.* 2011, 23, 3476–3485

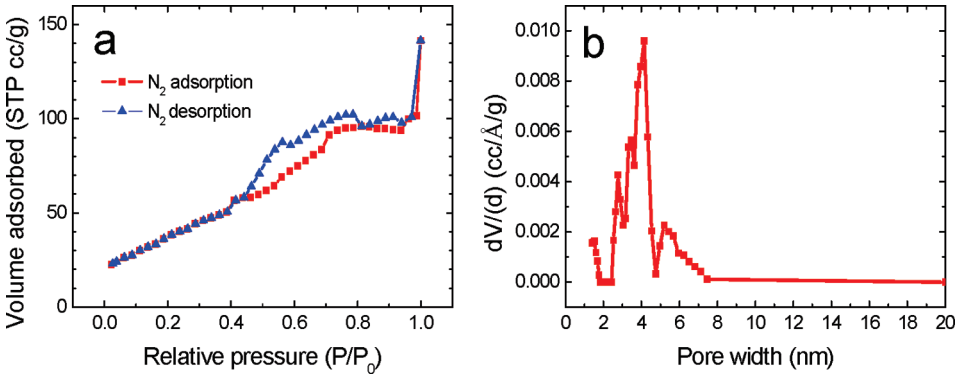

Figure 4. (a) Nitrogen isothermal adsorption/desorption data obtained from porous titania; the plot shows the amount of vapor adsorbed as a function of pressure up to one atmosphere. The sample was prepared by soaking PBT polymer fibers at 160 °C for 18 h in $TiCl_4$, then annealing at 450 °C for 12 h. (b) Pore size distribution of the porous titania calculated from the isotherm; the pore size is larger than that obtained for the same polymer soaked in TMA and annealed under the same conditions.

Some TMA could be left after water exposure, leading to slow hydrolysis upon air exposure. Upon closer inspection (inset in Figure 2b), pores 5−10 nm in size are readily visible, which is consistent with the pore size results discussed below. The EDS spectrum collected from the TEM sample shows aluminum, oxygen, and a trace amount of carbon. Altogether, the images show good microscopic uniformity after infiltration and thermal treatment.

We explored several metal-organic/polymer combinations and measured the specific surface area and pore size distribution using N_2 adsorption/desorption analysis. Table 1 summarizes the results. Results show that the pore size and size distribution are influenced by the soaking and calcination times, as well as the temperature. Figure 3a displays example nitrogen and hydrogen adsorption/desorption isotherms collected at 77 K after a 100-mg PBT fiber mat was soaked in TMA (18 h)/water (1 h) at 80 °C, then annealed for 12 h at 450 °C in air. The resulting BET surface area is ∼439 m^2/g, which is significantly larger than the 0.71 m^2/g value that was measured on untreated PBT fibers. The loop between the adsorption and desorption curve is correlated to Type E hysteresis, which is attributed to the present of "ink bottle" pores.[31] In addition, at 77 K and under atmosphere pressure, the treated sample can absorb 24.4 cm^3/g of hydrogen (at standard state), corresponding to ∼0.22 wt %. The topmost trace in Figure 3b provides information on the pore size distribution for this sample. The sample contains micropores with a pore width of ∼1 nm, along with mesopores with diameters in the range of 2−4 nm.

The TMA/water soak time strongly influences the final pore structure. The lower trace in Figure 3b shows that a TMA soak period of 1 h produces an average pore size of 5.45 nm, which is larger than that measured after an 18-h soak (3.23 nm). This average pore size is consistent with the cross-sectional TEM image in Figure 2b. We expect that the extended exposure time permits a more complete reaction between the metallorganic and the polymer, producing a tighter network with smaller pores. Smaller pores are also produced at higher infiltration/reaction temperature, as shown in Figure 3c, which is also consistent with a larger extent of metal-organic/polymer reaction. The results in Figure 3d show that, at a fixed reaction temperature of 80 °C, increasing the calcination temperature from 100 °C to 800 °C increases the average pore size and pore volume substantially. The increased pore size at high temperature could be induced, for example, by a more complete removal of the organic component and/or by pore reconstruction induced by alumina crystallization. Interestingly, the BET surface area results in Table 1 show that increasing infiltration temperature from 40 °C to 160 °C results in increases and decreases in the specific surface area. Increasing the process temperature will improve infiltration uniformity and produce smaller pores (increasing specific surface area), but on the other hand, more infiltration will increase the total mass and decrease the specific surface area. These two effects may not scale linearly, leading to the observed trends.

Interestingly, we find that the starting polymer repeat unit provides a template that shapes the pore size attained during calcination. Specifically, we treated PLA, PET, PBT, and PEN polyesters to the TMA sequential vapor infiltration for 18 h at 80 °C, followed by water exposure and calcination at 450 °C. The starting repeat unit lengths in PLA, PET, PBT, and PEN are 0.36, 0.86, 1.05, and 1.10 nm, respectively, and after processing, the corresponding average pore sizes were 1.41, 1.49, 3.22, and 2.68 nm, respectively. The polymers with larger repeat units tend to result in oxides with larger pores. In the above-mentioned set, the exception is for PBT, where the pores are larger than the monomer size trend would suggest. The PBT polymer is semicrystalline, and the crystal domains could impede TMA diffusion and reactivity, leading to regions of polymer that remain unreacted. Hence, slower diffusion kinetics in the crystalline phase will lead to larger pores after calcination. We explored this further by allowing the TMA infiltration into PBT to proceed for a longer time at higher temperature. If the kinetic limitation holds true, then pushing the reaction toward equilibrium (and saturation), will produce smaller pores. The results in Figures 3b and 3c support this hypothesis. Increasing the TMA soak time and/or temperature sharpens the peak and shifts it downward in size, demonstrating smaller and more-uniform pores. Soaking the PBT at 160 °C for 18 h produces pores that are ∼1.75 nm, which approaches the ∼1.05 nm PBT repeat unit length. Therefore, these results point to an explanation for the change in pore shape with infiltration time and temperature, and they suggest a practical approach to producing porous oxide materials with predetermined pore size and size distribution.

We also infiltrated $TiCl_4$ and diethyl zinc vapors into PBT, followed by calcination and characterization. Figure 4 shows

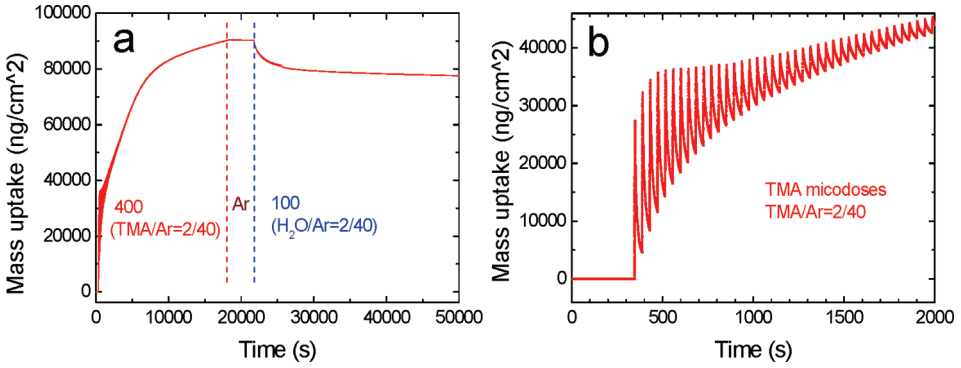

Figure 5. Mass increase during TMA/water infiltration at 80 °C on a cast PBT film, measured in situ using a quartz crystal microbalance. Panel a shows that the mass increase saturates after 400 microdoses (2 s each) of TMA, with an overall mass uptake of ~90 μg. This amount of mass increase is more than 1000 times larger than the ~40 ng measured for a typical TMA/water ALD process on a planar solid substrate (i.e., with no subsurface reaction). Similarly, the water reaction saturates after ~100 microdoses. Panel b shows a closer view of first 30 TMA microdoses on a PBT film. A large mass uptake occurs for the first several cycles and then decreases as exposure proceeds.

results from N_2 isothermal adsorption of mesoporous titanium dioxide obtained by exposing PBT to $TiCl_4$/water at 160 °C and annealing at 450 °C in air. We find that, under the same soak and calcination conditions, the $TiCl_4$ treatment produces a larger pore width (4.2 nm for $TiCl_4$ vs 1.75 nm for TMA). A similar increase in pore size results when PEN is exposed to $TiCl_4$ vs TMA (3.6 vs 2.7 nm, respectively). We expect that a slower reaction between the polyester and $TiCl_4$, compared to polyester/TMA, could produce a larger pore diameter.

Exposing PBT, PEN, and PBT to diethyl zinc and water vapor produced little reaction, and calcination yielded no measurable oxide residue. We hypothesize that the TMA or $TiCl_4$ adsorption sequence involves Lewis acid/base adduct formation at oxygen lone pair sites. DEZ is a weaker Lewis acid and is less likely to form the adduct state. Also, its larger size, compared to TMA and $TiCl_4$, also impedes diffusion into the polymer matrix.

In Situ Characterization of TMA/Water Infiltration of PBT. We applied in situ QCM and FTIR to monitor chemical interactions during vapor-phase polymer infiltration. For the QCM analysis, PBT was spun-coat onto quartz crystal substrates and mass uptake was measured upon exposure to a sequence of TMA and water vapor "micro-doses", consisting of exposure for 2 s, followed by a 40 s argon purge at 80 °C. After 400 TMA/argon microdose cycles, the reaction vessel was purged for 10 min, and then exposed to 100 water/argon microdoses with the same duration. The QCM results in Figure 5a show an initial large mass uptake, followed by saturation after ~400 microdoses, indicating reaction completion. After this, exposure to water/argon microdoses produces a net mass decrease, followed by saturation after ~100 dose steps. A closer view of data from the first 30 TMA/Ar cycles is displayed in Figure 5b, showing each TMA dose produced mass uptake, followed by mass decrease during each 40-s purge step. The mass decrease is ascribed to the desorption of TMA that is not tightly bound to the polymer. The total mass uptake recorded over 400 cycles is ~90 μg, which is significantly larger than that measured for a saturating exposure of TMA during Al_2O_3 ALD on a planar dense substrate (~40 ng).[30,32,33] The mass uptake confirms significant TMA interaction with the PBT film. The infrared data discussed below shows significant direct reaction. Since physisorbed or complexed TMA diffuses outward during the purge time, more is expected to be released during longer purges. The overall mass decrease during water exposure indicates a loss of organic composition,

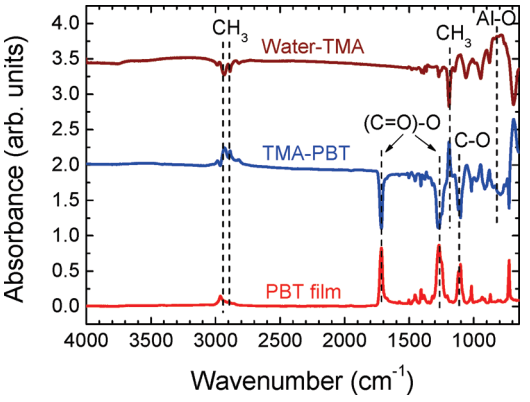

Figure 6. FTIR transmission spectra collected in situ from the a starting PBT film cast onto a silicon substrate (bottom trace) and after exposing the film to TMA (middle) and water (upper trace) at 80 °C. All spectra are displayed in differential mode where the previously collected spectrum was subtracted as the reference. The TMA exposure removes ester (1720 and 1270 cm^{-1}) and ether (1100 cm^{-1}) bonding units, indicating high reactivity between TMA and ester bonds in the PBT. The CH_3 (2860 and 2930 cm^{-1}) and Al-CH_3 modes (1200 cm^{-1}) increase upon TMA treatment, confirming the presence of Al−CH_3 in the soaked PBT film. After water dosing, the decrease in CH_3 and Al−CH_3 absorbance and an increase in Al−O modes shows water reacting with the Al−CH_3 groups to form Al−OH.

possibly through combustion reactions, to form Al−O−Al linkages. The reaction with water is discussed in more detail below. Interestingly, we found that removing the TMA-exposed samples from the reactor and exposing them to air could lead to spontaneous sample ignition, which is expected with pyrophoric TMA remaining within the fiber matrix. On the other hand, samples exposed to both TMA and water were stable in air and safe to handle.

Infrared transmission results provide insight into the reaction mechanisms, and Figure 6 displays results collected in situ during TMA and water soaking into a PBT film spun onto silicon. The spectrum for untreated polybutylene terephthalate (the bottom-most trace in Figure 6) displays modes for the C−O stretch at 1270 cm^{-1}, the C═O stretch at 1720 cm^{-1}, the C−O−C stretch at 1100 cm^{-1}, and the C−H_2 symmetric and asymmetric stretching at 2860 and 2925 cm^{-1}, respectively. The next trace

dx.doi.org/10.1021/cm200694w |*Chem. Mater.* 2011, 23, 3476–3485

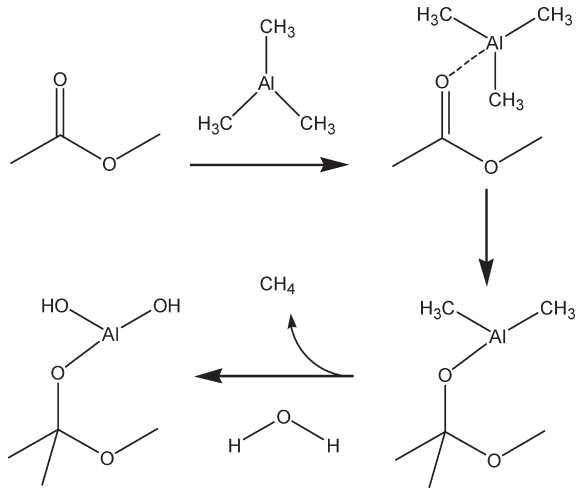

Figure 7. Proposed scheme for the PBT/TMA and PBT/TMA/water reactions consistent with the IR data shown in Figure 9. TMA is a strong Lewis acid and will likely attack nucleophilic carbonyl groups in the polyester to break the C═O ester bond and form aluminum alkyl oxide. Similarly, TMA can also insert itself into the C−O−C backbone linkage in the PBT to break the polymer chain and produce a methyl termination and a corresponding Al−$(CH_3)_2$ terminal group (not shown here). During water pulses, the Al−CH_3 groups readily react with water to form Al−OH.

shows the spectral change upon TMA exposure at 80 °C. In this case, TMA was allowed to flow in the reactor for 10 s, and then the reactor was sealed for 60 s. The system was then purged with argon, and data were collected during the argon purge step. The previous collected spectrum was subtracted as background, producing a differential spectrum. Negative-going modes at 1720 and 1270 cm^{-1} correspond to the removal of carbonyl stretching modes, and negative features at 1100 cm^{-1} indicate the removal of C−O−C groups. Positive signals at 2960 cm^{-1} and 1200 cm^{-1} indicate the appearance of CH_3 stretching features, which are indicative of the methyl groups on TMA. A new mode at 680 cm^{-1} is ascribed to Al−C bonds formed upon the TMA reaction. These changes demonstrate that TMA reacted with the carbonyl group on the PBT to form C−O−Al−$(CH_3)_2$ and C−CH_3 groups. During the following water exposure, Al−CH_3 features were removed, producing an increase in Al−O stretching modes in the ∼800 cm^{-1} range, which is consistent with water reacting with Al−CH_3 groups.

Reactions during the TMA and Water Vapor Exposure Steps. The topmost spectrum in Figure 6 was collected after the water vapor exposure step at 80 °C, following the same cycle timing used for TMA/argon. This shows the removal of Al−CH_3 modes and the formation of Al−O and OH features. A simplified scheme showing possible reactions between the PBT, trimethyl aluminum, and water is shown in Figure 7. Trimethyl aluminum could attack nucleophilic carbonyl groups in the polyester to break the C═O ester bond, resulting in a methyl group transfer to the carbonyl carbon and the formation of aluminum alkyl oxide.[34] Computational results from Derk et al.[35] predict that the reaction between TMA and the ester group in methyl acetate will react exothermically through 1,2-carbonyl addition with an overall heat of reaction of −32.7 kcal/mol. This is almost as large as the −36.8 kcal/mol heat of reaction that is predicted for the hydroxylation of TMA by water to produce methane. Analogous to the carbonyl insertion reaction proposed, the in situ FTIR spectra suggested an additional reaction between trimethyl aluminum and PBT may involve TMA insertion into ether linkages in the polymer backbone, to break the polymer chain and produce a carbon−methyl termination and a corresponding −O−Al−$(CH_3)_2$ terminal group. Derk et al. also calculated the reaction between TMA and dimethyl ether to form $(CH_3)_2$−Al−O−CH_3 and ethane,[35] and they found it to be overall exothermic, with an overall heat of reaction of −38.7 kcal/mol. However, the reaction is predicted to proceed through a relatively high-energy transition state, which could impede the net reaction kinetics. During water pulses, the Al−CH_3 groups readily react with water to form Al−OH, or undergo other reactions to form Al−O−Al network bonds.

The reaction between TMA/water and polyester could also produce volatile organic species that could diffuse outward from the polymer bulk. For example, further hydrolysis of −Al−O−$[CH_2]_4$−O−Al− units could produce a volatile diol (e.g., butylene glycol is a monomer used to form PBT). This outward diffusion of vapor products during the water exposure step would explain the decrease in overall sample size that is observed in Figure 1a, and it may help to produce diffusion pathways through any outer alumina layers to enable water to access the polymer fiber bulk region. Previous research confirms that organic species evolution occurs upon the hydrolysis of metal oxide/polymer hybrid films prepared by molecular layer deposition.[29,36,37] This is also consistent with our BET results. Untreated PBT is stable upon annealing at 100 °C, but after TMA infiltration at 80 °C, annealing at 100 °C produces porous materials with specific surface areas of >100 m^2/g (see Table 1). This is explained by the volatilization of products formed during reaction with TMA/water.

Even though the reaction would result in the breaking of polymer chains, since the polymer retains its macroscopic physical shape, some interconnection must remain after the TMA reaction step. One possibility is that the TMA reaction with the ester group impedes reaction of a neighboring ester and thereby helps to retain the network structure. Also after insertion, a bonded −O−Al−CH_3 group may further react with adjacent ester groups to form new −O−Al−O− interconnections. These new interconnections would explain why the polymer retains its macroscopic shape after infiltration and subsequent calcination.

Chemical and Thermal Analysis of Infiltrated Materials. After fully reacting PBT in TMA/water (before calcination), XPS analysis showed an Al:C atomic ratio of ∼1:3 (12.7 at.% Al, 37.2 at.% C), confirming significant aluminum infiltration. The C 1s spectral features collected before and after processing (see Figure 8) confirm the removal of C═O and the formation of C−O−Al. The TMA/water-soaked PBT fiber (before calcination) is X-ray amorphous, with no diffraction peaks detected. Figure 9 shows differential sanning calorimetry (DSC) and TGA analysis of untreated and SVI-treated PBT fibers (without calcination). The DSC analysis of the untreated PBT shown in Figure 9a indicates a clear increase of heat flow at ∼220 °C, which is consistent with the expected melting point (T_m) for PBT. The TGA analysis of untreated PBT fibers (see Figure 9b) exhibited >90% mass loss at ∼400 °C and 100% loss by 525 °C. The DSC trace in Figure 9c for the SVI-treated PBT showed no obvious T_m value, further revealing disruption of the polymer structure by TMA/water infiltration. This sample also showed continuous mass loss with ∼25% remaining after heating to 900 °C. In principle, one may expect that if the TMA/water fully reacted with all the carbonyl groups in the polymer chain, it could

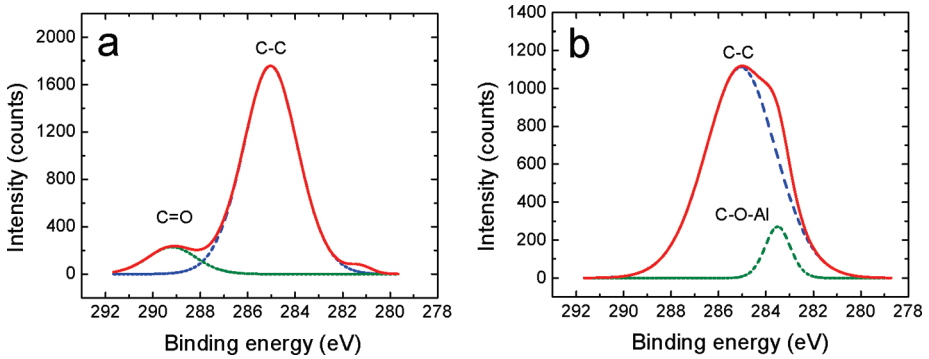

Figure 8. X-ray photoelectron spectroscopy (XPS) spectra of the C 1s feature in (a) an untreated PBT film and (b) a PBT film after TMA/water infiltration. The spectra collected after TMA/water infiltration show negligible C═O at ∼289 eV and the formation of Al−O−C at ∼283.5 eV, which is consistent with the mechanism shown in Figure 7.

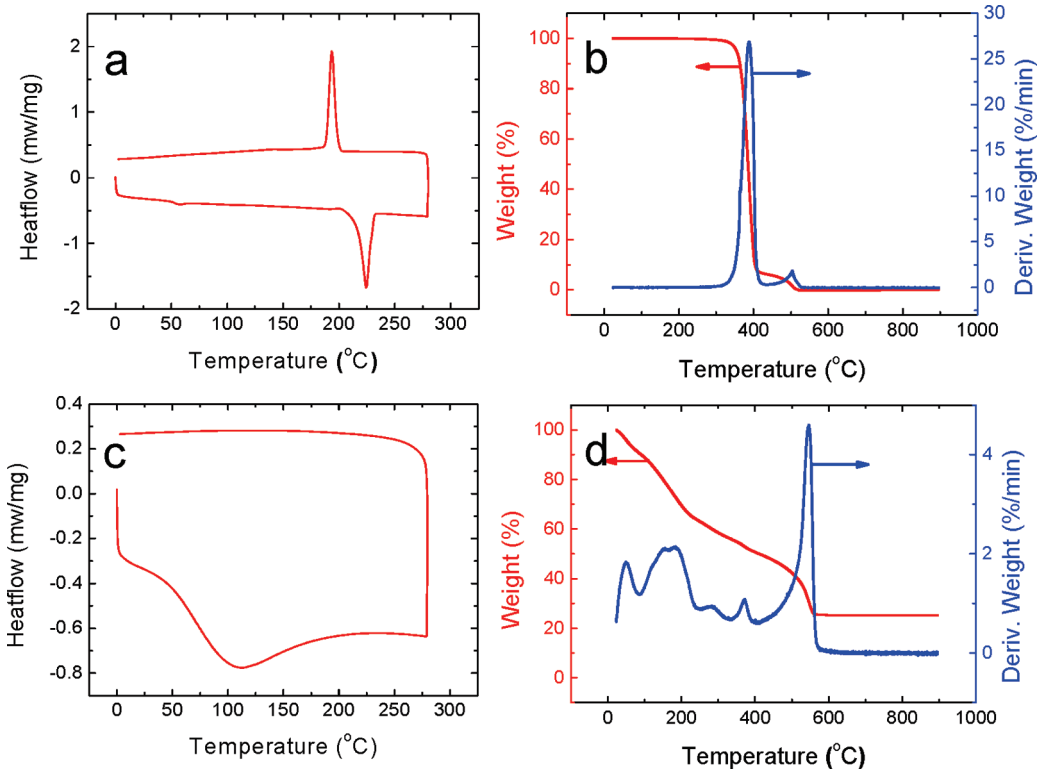

Figure 9. Differential scanning calorimetry (DSC) and thermogravimetric analysis (TGA) of (a,b) untreated PBT fibers and (c,d) TMA/water-infiltrated PBT fibers. Results in panel a show increased heat flow at ∼220 °C, which is consistent with the PBT melting point. Whereas, in panel c, for the TMA/water-soaked PBT, no obvious T_m value was observed up to 275 °C. The TGA curve for untreated PBT in panel b shows a rapid mass decrease at ∼400 °C, with ∼0% residue after 900 °C. However, after TMA/water soaking, panel d shows a more gradual mass loss, continuing until ∼550 °C with ∼25% of the mass remaining after 900 °C.

result in a uniform microporous structure with an average pore size that is comparable to the nanometer or subnanometer dimension of the remaining organic groups. The 25% remaining mass observed by TGA indicates a larger organic fraction, which is consistent with mesopores a few nanometers in size.

The thermal and ambient stability of the material after infiltration is also of interest. Figure 10 shows ex situ FTIR analysis of a PBT film soaked in TMA/water at 80 °C, immediately after removing it from the reactor and after several hours in ambient laboratory air. The as-soaked material shows modes associated with CH_3 and CH_2 stretching, and a broad absorbance band centered near 700 cm^{-1} due to Al−O stretching vibrations. After 1 h of air exposure, a significant increase in hydroxyl group absorption is observed between 3000 and 3700 cm^{-1} due to moisture uptake from the ambient. With extended exposure, the hydroxyl group intensity stays relatively stable, but a continued decrease of organic-related mode intensity is evidence for continued volatilization of the organic component. This could result from the reaction between moisture and unreacted TMA in the polymer substrate and/or the evaporation of volatile products formed during hydrolysis. The topmost spectrum in Figure 10 obtained from the sample after annealing for 120 min

dx.doi.org/10.1021/cm200694w |*Chem. Mater.* 2011, 23, 3476–3485

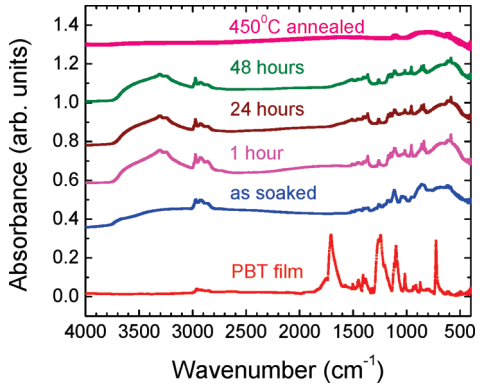

Figure 10. Ex situ FTIR spectra showing the ambient and thermal stability of a TMA/water-infiltrated PBT film. The TMA/water-soaked PBT continues to absorb water from the ambient during 1 h of air exposure. Annealing at 450 °C removes water and the organic component, leaving primarily Al−O modes near 700 cm^{-1}.

in air at 450 °C shows only Al−O stretching, demonstrating the formation of an Al_2O_3 matrix.

IV. CONCLUSIONS

This work demonstrates a new approach for the synthesis of shape-controlled microporous/mesoporous materials using polyesters as sacrificial templates. Vapor-phase trimethyl aluminum (TMA) and titanium tetrachloride precursors can diffuse into polyester fibers, including polybutylene terephthalate (PBT), polyethylene terephthalate (PET), polylactic acid (PLA), and polyethylene naphthalate (PEN), and using water as a co-reactant, to produce a matrix network hybrid organic−inorganic polymer. This polymer readily transforms upon annealing in air to yield a porous inorganic Al_2O_3 or TiO_2 solid monolith. Moreover, the shape and macroscopic physical appearance of the inorganic solid faithfully duplicates that of the original starting polymer. The proposed reaction sequence during TMA/water exposure on PBT involves a large TMA mass uptake and removal of (C═O)−O bonding units through TMA interaction with the ester bond in the PBT backbone, likely through Lewis acid/base adducts. Experiments using a relatively weak Lewis acid such as diethyl zinc as the metal source do not produce similar reactions, which is consistent with the proposed reaction mechanism. The microporous/mesoporous structure is confirmed using cross-sectional transmission electron microscopy and nitrogen absorption/desorption experiments. The pore size and volume depend systematically on the detailed process conditions. The data show that the starting polymer repeat unit acts to template the resulting inorganic pore size. The ability to prepare porous inorganic solids with tunable pore size, where the monolith shape is preselected by the shape of the starting polymer template, could be useful for catalytic support structures, chemical and electrochemical separations, and other porous membrane systems. This process is also open to a wide range of inorganic components and a variety of different starting polymers, allowing significant versatility over the final product design.

AUTHOR INFORMATION

Corresponding Author

*Tel.: 919 5157553. E-mail: parsons@ncsu.edu.

ACKNOWLEDGMENT

This project was funded through the U.S. National Science Foundation (under Grant No. 1034374).

REFERENCES

(1) Corma, A. *Chem. Rev.* **1997**, *97*, 2373.
(2) Solerillia, G. J. D.; Sanchez, C.; Lebeau, B.; Patarin, J. *Chem. Rev.* **2002**, *102*, 4093.
(3) Zhao, D. Y.; Feng, J. L.; Huo, Q. S.; Melosh, N.; Fredrickson, G. H.; Chmelka, B. F.; Stucky, G. D. *Science* **1998**, *279*, 548.
(4) Zhao, D. Y.; Huo, Q. S.; Feng, J. L.; Chmelka, B. F.; Stucky, G. D. *J. Am. Chem. Soc.* **1998**, *120*, 6024.
(5) Eddaoudi, M.; Moler, D. B.; Li, H. L.; Chen, B. L.; Reineke, T. M.; O'Keeffe, M.; Yaghi, O. M. *Acc. Chem. Res.* **2001**, *34*, 319.
(6) Li, H.; Eddaoudi, M.; O'Keeffe, M.; Yaghi, O. M. *Nature* **1999**, *402*, 276.
(7) Rosi, N. L.; Eckert, J.; Eddaoudi, M.; Vodak, D. T.; Kim, J.; O'Keeffe, M.; Yaghi, O. M. *Science* **2003**, *300*, 1127.
(8) Yaghi, O. M.; O'Keeffe, M.; Ockwig, N. W.; Chae, H. K.; Eddaoudi, M.; Kim, J. *Nature* **2003**, *423*, 705.
(9) Cote, A. P.; Benin, A. I.; Ockwig, N. W.; O'Keeffe, M.; Matzger, A. J.; Yaghi, O. M. *Science* **2005**, *310*, 1166.
(10) El-Kaderi, H. M.; Hunt, J. R.; Mendoza-Cortes, J. L.; Cote, A. P.; Taylor, R. E.; O'Keeffe, M.; Yaghi, O. M. *Science* **2007**, *316*, 268.
(11) Han, S. S.; Furukawa, H.; Yaghi, O. M.; Goddard, W. A. *J. Am. Chem. Soc.* **2008**, *130*, 11580.
(12) Wood, C. D.; Tan, B.; Trewin, A.; Niu, H. J.; Bradshaw, D.; Rosseinsky, M. J.; Khimyak, Y. Z.; Campbell, N. L.; Kirk, R.; Stockel, E.; Cooper, A. I. *Chem. Mater.* **2007**, *19*, 2034.
(13) Budd, P. M.; Ghanem, B. S.; Makhseed, S.; McKeown, N. B.; Msayib, K. J.; Tattershall, C. E. *Chem. Commun.* **2004**, 230.
(14) Germain, J.; Hradil, J.; Frechet, J. M. J.; Svec, F. *Chem. Mater.* **2006**, *18*, 4430.
(15) Tozawa, T.; Jones, J. T. A.; Swamy, S. I.; Jiang, S.; Adams, D. J.; Shakespeare, S.; Clowes, R.; Bradshaw, D.; Hasell, T.; Chong, S. Y.; Tang, C.; Thompson, S.; Parker, J.; Trewin, A.; Bacsa, J.; Slawin, A. M. Z.; Steiner, A.; Cooper, A. I. *Nat. Mater.* **2009**, *8*, 973.
(16) Bezzu, C. G.; Helliwell, M.; Warren, J. E.; Allan, D. R.; McKeown, N. B. *Science* **2010**, *327*, 1627.
(17) Sozzani, P.; Bracco, S.; Comotti, A.; Ferretti, L.; Simonutti, R. *Angew. Chem., Int. Ed.* **2005**, *44*, 1816.
(18) Lim, S.; Kim, H.; Selvapalam, N.; Kim, K. J.; Cho, S. J.; Seo, G.; Kim, K. *Angew. Chem., Int. Ed.* **2008**, *47*, 3352.
(19) Zacher, D.; Shekhah, O.; Woll, C.; Fischer, R. A. *Chem. Soc. Rev.* **2009**, *38*, 1418.
(20) Li, D.; Wang, Y. L.; Xia, Y. N. *Nano Lett.* **2003**, *3*, 1167.
(21) Madhugiri, S.; Sun, B.; Smirniotis, P. G.; Ferraris, J. P.; Balkus, K. J. *Microporous Mesoporous Mater.* **2004**, *69*, 77.
(22) RomanC., G. T.; Culbertson, T. *Langmuir* **2006**, *22*, 4445.
(23) Roman, G. T.; Hlaus, T.; Bass, K. J.; Seelhammer, T. G.; Culbertson, C. T. *Anal. Chem.* **2005**, *77*, 1414.
(24) Wilson, C. A.; Grubbs, R. K.; George, S. M. *Chem. Mater.* **2005**, *17*, 5625.
(25) Hyde, G. K.; Scarel, G.; Spagnola, J. C.; Peng, Q.; Lee, K.; Gong, B.; Roberts, K. G.; Roth, K. M.; Hanson, C. A.; Devine, C. K.; Stewart, S. M.; Hojo, D.; Na, J. S.; Jur, J. S.; Parsons, G. N. *Langmuir* **2010**, *26*, 2550.
(26) Zhang, L. B.; Patil, A. J.; Li, L.; Schierhorn, A.; Mann, S.; Gosele, U.; Knez, M. *Angew. Chem., Int. Ed.* **2009**, *48*, 4982.
(27) Lee, S. M.; Pippel, E.; Gosele, U.; Dresbach, C.; Qin, Y.; Chandran, C. V.; Brauniger, T.; Hause, G.; Knez, M. *Science* **2009**, *324*, 488.
(28) Lee, S. M.; Pippel, E.; Moutanabbir, O.; Gunkel, I.; Thurn-Albrecht, T.; Knez, M. *ACS Appl. Mater. Interfaces* **2010**, *2*, 2436.
(29) Peng, Q.; Gong, B.; VanGundy, R. M.; Parsons, G. N. *Chem. Mater.* **2009**, *21*, 820.

(30) Spagnola, J. C.; Gong, B.; Arvidson, S. A.; Jur, J. S.; Khan, S. A.; Parsons, G. N. *J. Mater. Chem.* **2010**, *20*, 4213.
(31) Thommes, M.; Smarsly, B.; Groenewolt, M.; Ravikovitch, P. I.; Neimark, A. V. *Langmuir* **2006**, *22*, 756.
(32) Elam, J. W.; Groner, M. D.; George, S. M. *Rev. Sci. Instrum.* **2002**, *73*, 2981.
(33) Leskelä, M. *Thin Solid Films* **2002**, *409*, 138.
(34) Peng, Q.; Tseng, Y. C.; Darling, S. B.; Elam, J. W. *Adv. Mater.* **2010**, *22*, 5129.
(35) Derk, A. R.; Zimmerman, P.; Musgrave, C. B. Reactivity of Trimethylaluminum Towards Organic Functional Groups for the Deposition of Hybrid Organic−Inorganic Films by Molecular and Atomic Layer Deposition. Unpublished work, 2010.
(36) Dameron, A. A.; Seghete, D.; Burton, B. B.; Davidson, S. D.; Cavanagh, A. S.; Bertrand, J. A.; George, S. M. *Chem. Mater.* **2008**, *20*, 3315.
(37) Gong, B.; Peng, Q.; Parsons, G. N. *J. Phys. Chem. B* **2011**, *115*, 5930.